JOURNAL OF PROPULSION AND POWER
Vol. 25, No. 6, November–December 2009

Numerical Simulation of SMART-1 Hall-Thruster Plasma Interactions

Martin Tajmar,* René Sedmik,† and Carsten Scharlemann‡
Austrian Institute of Technology, GmbH, A-2444 Seibersdorf, Austria

DOI: 10.2514/1.36654

SMART-1 has been the first European mission using a Hall thruster to reach the moon. An onboard plasma diagnostic package allowed a detailed characterization of the thruster exhaust plasma and its interactions with the spacecraft. Analysis of in-flight data revealed, amongst others, an unpredicted large cyclic variation of the spacecraft floating potential and a mysterious asymmetry in the plasma surrounding the spacecraft. To investigate the details of the anomalies, we developed the numerical software tool SmartPIC to characterize and predict spacecraft–plasma interactions. Technical details, such as solar arrays and onboard diagnostic devices, have been modeled with high accuracy. All basic plasma parameters, the spacecraft floating potential, backflow distributions, and ion impact energies are calculated by the code and are available in high spatial resolution throughout the computational domain containing the entire satellite. It was possible to clearly identify the rotating solar cells arrays as the source of the cyclic variation of the spacecraft floating potential. Furthermore, the asymmetry of the plasma formation around the spacecraft is linked to the location of the neutralizer causing a region of increased charge-exchange collisions particle generation. Both of these results have significant impact on the implementation of electric propulsion systems on satellites.

Nomenclature

d = geometric distance
e = electron charge, 1.60217×10^{-19} C
I_E = thruster ion current
$I_{B,I/E}$ = ion/electron backflow current
I_N = neutralizer electron current
k_B = Boltzmann constant, 1.38065×10^{-23} J/K
$\dot{m}$ = total mass flow
m_e = electron mass, 9.10938×10^{-31} kg
m_i = xenon ion mass, 2.19901×10^{-25} kg
n_e, n_i, n_{CEX} = electron, ion, and charge-exchange collisions ion densities
$P_{i,j}$ = collision probability
PPP_α = particle per superparticle ratio, 10^8–10^{10}
r_i, r_o = radii, 28, 50 mm
s_{cath} = cathode mass flow ratio, 8%
T_e, T_i, T_{CEX} = electron, ion and charge-exchange collisions particle temperatures
U_{acc} = thruster acceleration voltage, 350 V
v, Δv = velocities, differences of
Z = charge multiplier, one or two
α = solar array rotation angle
α_i, α_o = geometry angles
Δt = time step
ε_0 = permittivity of vacuum, 8.85419×10^{-19} F/m
η_{double} = relative fraction of double charged ions, 10%
η_{ion} = ionization efficiency, 95%
$\eta_{\mathrm{sh,ic/diel}}$ = shielding coefficient for interconnectors/glass, varies
λ_D = debye length
σ_{ij} = collision cross section
ϕ, ϕ_P = local plasma potential
ϕ_{CEX} = charge-exchange plasma potential
ϕ_f = spacecraft floating potential
ϕ_{SC} = spacecraft surface potential

I. Introduction

BACK in 2003, ESA started an ambitious program called SMART (Smart Missions for Advanced Research and Technology), which is dedicated to the development and demonstration of innovative concepts needed for future precursor missions, such as Bepi Colombo. The focus lies on propulsion, energy, sensor technology, and autonomous systems. SMART-1 has been the premiere satellite within the framework. Its main purpose was the demonstration of an electric propulsion system applied as the primary drive for an interplanetary mission. SMART-1 was equipped with a PPS-1350 Hall thruster built by Societe Nationale d'Etude et de Construction de Moteurs d'Aviation, providing a constant thrust of 70 mN. In addition, several ambitious targets, such as tests of high-resolution spectroscopy, autonomous navigation systems, and geophysical imaging, have been achieved.

Electric propulsion is known to produce low-energetic ions resulting from scattering within the exhaust plume that can easily be redirected toward the satellite. On impact, these particles cause spacecraft surface degradation and might lead to differential surface charging. To investigate and characterize the plasma environment, SMART-1 was equipped with an electric propulsion diagnostic package (EPDP) and the so-called spacecraft potential electron and dust experiment (SPEDE). These instruments enabled the analysis of plasma densities and plasma energies as well as the measurement of the spacecraft floating potential relative to the surrounding plasma.

It has been a major objective of the mission to achieve an in-depth understanding of the physics governing the plasma environment around the satellite. Therefore, ESA initiated a working group including European companies and research institutes to study plasma spacecraft interactions on SMART-1. The present paper summarizes our efforts which led to the development of the plasma and spacecraft interaction simulation tool SmartPIC.

Received 14 January 2008; revision received 28 August 2009; accepted for publication 2 September 2009.

*Head of Department, Space Propulsion and Advanced Concepts; also Lecturer, Institute of Lightweight Design and Structural Biomechanics, Vienna University of Technology, A-1040 Vienna, Austria; martin.tajmar@ait.ac.at. Member AIAA.

†Ph.D. Student; currently Vienna University of Technology, A-1040 Vienna, Austria; sedmik@hep.itp.tuwien.ac.at.

‡Deputy Head of Department, Space Propulsion and Advanced Concepts; carsten.scharlemann@ait.ac.at. Member AIAA.

Basic information about the satellite is given in Sec. II. Effects caused by backflow plasma are shortly reviewed in Sec. III. The physical model and the implementation of SmartPIC are discussed in Secs. IV.A and IV.B, respectively. Results and methodology of the extensive code verification are given in Sec. V, and results of electric propulsion plasma investigations are discussed subsequently in Sec. VI. Finally, the project is summarized in Sec. VII.

II. SMART-1 Satellite

The main body of SMART-1 is of approximately cubic shape ($l \times w \times h = 1110 \times 1110 \times 905$ mm). As shown in Fig. 1, the electric thruster is situated on the top ($+Z$ plane), mounted in a circular cavity. On the $\pm Y$ planes, rotatable extension arms of 900 mm length attach the two solar arrays to the satellite's main body. The arrays are each divided into three panels of equal size. Each panel has six sections (in Y direction) which consists of three strings (in X direction). The strings again are placed such that the voltage increases meander shaped from 0 V to a maximum of 50 V along five substrings. These are connected at their ends via so-called interconnectors of 8 mm width. Figure 2 shows a sketch of this complex geometric structure.

Figure 1 shows the position of the EPDP consisting of a retarding potential analyzer (RPA) and a langmuir probe (LP). The EPDP LP is a truncated sphere of 7.5 mm diameter mounted on a few-centimeters-long support. The instrument is located within a region of high-intensity backflow which enables an analysis of the diffuse plasma cloud with impact energies <100 eV. A solar array sample designed as a probe to measure degradation effects is located on the opposite $-Z$ panel. As shown in Fig. 1, the two single-ended LPs of SPEDE were mounted on 60-cm-long booms on the $\pm X$ side of the satellite. Featuring a fast capture mode, the instrument enables the observation of plasma waves as well as precise measurements of electron and ion densities.

III. Effects of Electric Propulsion

The plasma expelled by an electric thruster represents an electrically active component that sensitively interacts with the spacecraft. The most significant impact comes from slow ions, which are created by collisions of beam particles in the exhaust with slow neutral propellant or ambient gas (so-called charge-exchange collisions or CEX). In such processes, charge is transferred from ions to neutrals without any change of momentum. The resulting low-energetic CEX ions are easily redirected toward the spacecraft by negative electric potentials, which results in sputtering on surfaces, material deposition, and electric charging effects. Subsequent differential charging of spacecraft surfaces may trigger discharges resulting in, for example, erroneous measurements or damaged equipment (sensors, electronic devices, or solar cells).

On SMART-1, the EPDP and SPEDE instruments have been operated in frequent intervals, allowing a complete characterization of the plasma surrounding the satellite. One of the main features

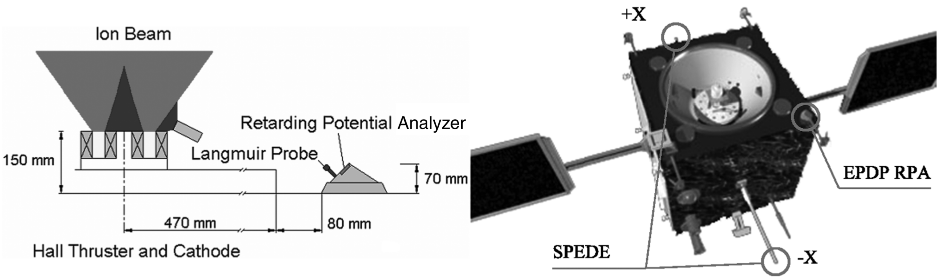

Fig. 1 EPDP and SPEDE positions on the satellite.

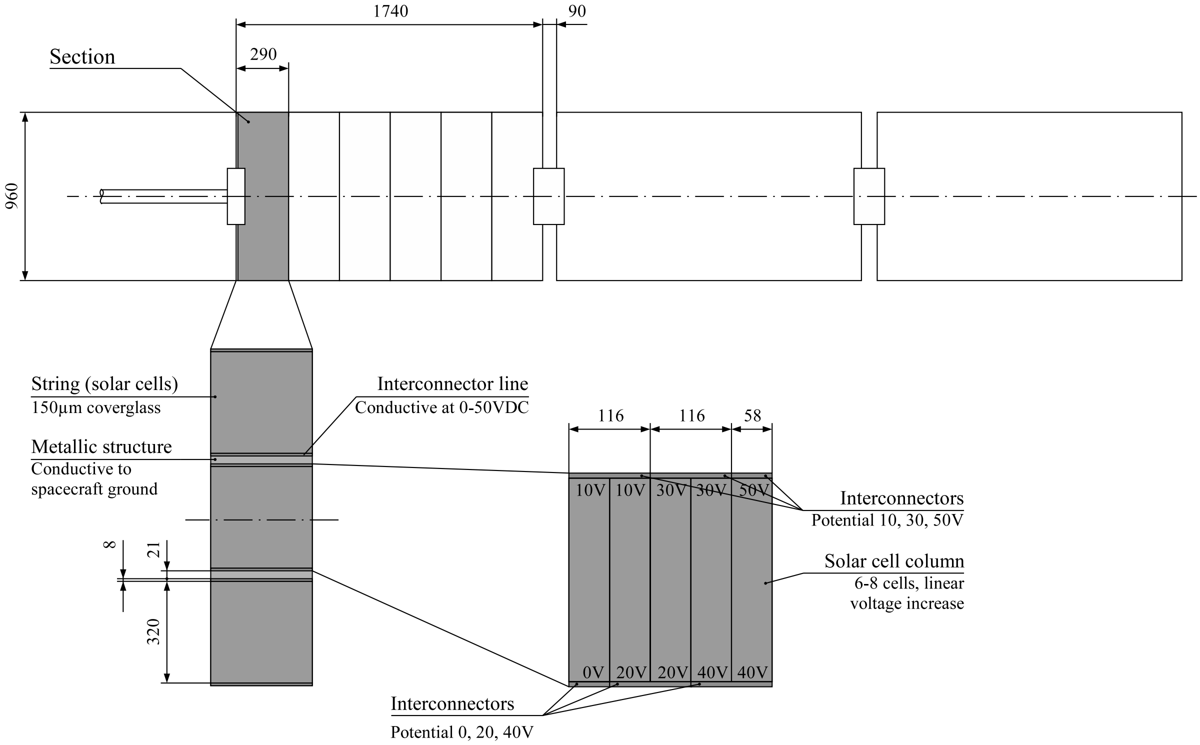

Fig. 2 Illustration of the solar array structure used in SmartPIC. The scheme represents only a slight simplification compared to the real structure on SMART-1.

shown by these measurements regards the backflow distribution. High particle densities of 10^{13}–10^{14} m^{-3} have been measured at the $+Z$ side of the main body by the EPDP LP. Peak energies at this position were around 18.5 eV which, compared to ~350 eV of primary beam ions, clearly indicates that the measured plasma species represent CEX backflow. In addition, SPEDE measurements were used to characterize the low-density backflow and environmental plasma at intermediate distances from the thruster, showing densities around 10^{8-10} m^{-3}. More details on these measurements and comparison to numerical results are presented in Secs. V and VI.

The onboard measurements on SMART-1 also showed two effects that could not be anticipated a priori. SPEDE measurements on the $+X$ and $-X$ panel exhibited a clear asymmetry in the plasma distribution being reflected in the current on the $-X$ panel being always ~5% higher than on the $+X$ panel. The nearly symmetric construction of the satellite gives no indication for the reason of this anomaly, and the reason for this phenomenon was unclear. The second unexpected phenomenon was a cyclic variation of the spacecraft floating potential ϕ_f over time, approximately correlated with the orbital position of the satellite. The latter relation gave rise to discussions on possible reasons, including Fig. 3: 1) photo effect and secondary electron emission due to hard radiation from the sun, 2) orbit-local dense plasma configurations, and 3) interaction of the solar arrays with the thruster plasma backflow.

None of these processes could easily be excluded or confirmed to be responsible for the variations. However, a peculiar coincidence was recognized after a detailed investigation of the satellite's telemetry. The cyclic variation of the floating potential seems to coincide with the change in the solar array position. Figure 3 shows an example for in-flight measurements of the EPDP floating potential, which is directly related to the spacecraft ground and, therefore, ϕ_f. In the figure, the panel rotation is indicated by the solar array normal angle relative to the $+Z$ axis.

The investigation of this correlation and the search for physical reasoning for all the effects mentioned previously have been one of the main objectives for SmartPIC. Thorough numerical simulation required detailed geometric and physical modeling of SMART-1 at high spatial resolution throughout a large computational domain.

IV. Simulation Model

A. Physical Model

The plasma in the beam of a Hall thruster typically has number densities $>10^{15}$ m^{-3}. Hence, it is not possible to use brute-force methods which simulate physical particles. Instead, the widely used PIC approach is applied. So-called superparticles representing a number of 10^8–10^{10} real particles are introduced. In that way, the total number of simulated entities of Xe, Xe$^+$, and Xe^{2+} is kept below 10^6, thereby rendering the simulation computable on standard workstations. Electrons and background neutrals are implemented by another approach, representing the respective species solely by densities on the underlying computational grid.

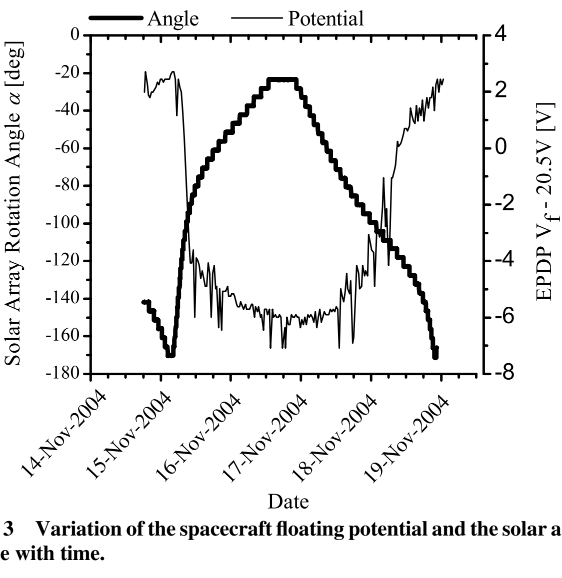

Fig. 3 Variation of the spacecraft floating potential and the solar array angle with time.

New particles are introduced at the thruster exit at a constant velocity

$$v_i = \sqrt{\frac{2eZU_{\mathrm{acc}}}{m_i}} \tag{1}$$

Although a Gaussian distribution might be more physically sound, in the present case, the assumption of constant ion energy was chosen. As will be shown later, in Sec. V, the only effect of this simplification are smaller peaks for ion densities in RPA results. According to the ratio of real particles per superparticle for a species α, PPP_α, the number of ions Δn introduced per time step Δt is derived from the emitter ion current I_{ie} by

$$\Delta n_i = \frac{I_{\mathrm{ie}}}{PPP_i}\Delta t \quad \text{with } I_{\mathrm{ie}} = \begin{cases} \frac{\dot{m}(1-s_{\mathrm{cath}})\eta_{\mathrm{ion}}}{m_i(1+2\eta_{\mathrm{double}})} & \text{single charged} \\ \frac{\dot{m}(1-s_{\mathrm{cath}})2\eta_{\mathrm{double}}\eta_{\mathrm{ion}}}{m_i(1+2\eta_{\mathrm{double}})} & \text{double charged} \end{cases} \tag{2}$$

The prefactor 2 in the denominator is reasoned by the fact that η_{double} *is* a number fraction, but the normalization is associated with the electric current. Similar relations with $(1 - s_{\mathrm{cath}})$ replaced by s_{cath} hold for the number of particles inserted at the cathode.

The initial positions of ions are uniformly distributed across the thruster opening between the inner radius r_i and the outer radius r_o. The direction of the velocity v_i is determined in spherical coordinates $(v_i; \alpha_1; \alpha_2)$, where α_1 is chosen by random between $0 < \alpha_1 < 2\pi$, and α_2 is varied in accordance to the radial position between the inner and outer beam-spreading angles α_i and α_o by

$$\alpha_2(r) = \frac{\alpha_i - \alpha_o}{r_o - r_i}(r - r_i) + r_i \tag{3}$$

In addition, a stochastic thermal component is added to this geometrically exact distribution. It consists of an axial and a radial component, both determined by a Boltzmann distribution which is parameterized by axial and radial temperatures $T_{i,\mathrm{ax}}$ and $T_{i,\mathrm{rad}}$, respectively.

The PPS-1350 features a hollow cathode neutralizer. Because of the limited efficiency of this device, a constant flux of xenon particles is created over the neutralizer exit area. The number of neutrals appearing at this position in a uniform distribution is

$$\Delta n_{n,em} = \frac{I_{mn,em}}{PPP_n}\Delta t \quad \text{with } I_{mn,em} = \frac{\dot{m}(1 - s_{\mathrm{cath}})}{m_n}(1 - \eta_{\mathrm{ion}}) \tag{4}$$

At the thruster exit, neutrals are inserted in the same way as ions because they are not affected by the electric field, the velocity of neutral particles is solely determined by the thermal distribution.

Electrons are principally represented by their number density which is determined by the quasi-neutrality assumption ($n_e = n_i$). This simplification is applicable to plasmas of sufficiently high density not being subjected to high external electric fields. These assumptions are, however, questionable in the case of a satellite because local surface potentials cause electric fields, and the density outside the beam in the vicinity of the solar array drops by at least four orders to $n_e \approx 10^{12}$ m^{-3}. On the other hand, relaxing quasi neutrality implies treating all particle species in a purely kinetic manner, governed by the Poisson equation, as has been done by Hastings and Chang [2], and Szabo [3]. For a computational domain enclosing an object of the size of a satellite, this is not feasible due to excessive amount of memory needed for such a computation. Therefore, the only viable way is to allow quasi neutrality and take advantage of the Boltzmann relation [1]:

$$\phi_P = \frac{k_B T_e}{e} \ln\left(\frac{n_e}{n_{e,0}}\right) + \phi_0 \tag{5}$$

It relates the electron density to the local plasma potential ϕ_P, provided a reference density $n_{e,0}$ and the respective potential ϕ_0 are known at some point. The electron temperature can be determined according to an adiabatic energy model

$$k_B T_e n_e^{-\gamma+1} = C_1 \tag{6}$$

where $\gamma = 1.28$ and $C_1 = 8.76 \times 10^{-5}$ are derived from experimental results [4]. Equation (5) can only be applied to regions without perturbating electric fields. In principal, the total potential should be calculated using the Poisson equation

$$\nabla^2 \phi = \varepsilon_0 e (n_i - n_e) \tag{7}$$

However, presuming $n_e = n_i$ prohibits the use of this approach. Therefore, in SmartPIC, the approach is to determine the total potential by superposing a static solution obtained by first solving for the free space potential ϕ_{SC} with the spacecraft surface potentials entering as Dirichlet boundary conditions and no plasma effects. Equation (7) therefore reduces to a Laplace equation $\nabla^2 \phi_{\text{SC}} = 0$. In a second step, the local plasma potential is determined by Eq. (5) and finally superposed with the static solution

$$\phi = \phi_{\text{SC}} + \phi_P \tag{8}$$

This approximation is valid if electric fields $E = -\nabla\phi$ emitted by the spacecraft stay small, which is guaranteed throughout the computational domain except in the direct vicinity of surfaces.

Collisions play an important role in the simulation because they are the source for plasma backflow to the spacecraft. The collision model implements two different methods. The first one is used if the primary particle is much faster than the secondary population, which is the case for ions and background neutrals [Monte Carlo collision (MCC)]. The other method chooses two explicit particles and collides them [direct simulation Monte Carlo (DSMC)]. The MCC algorithm, in our case, changes the fast ion particle into a slow charge-exchange ion, giving it a random direction and a speed according to the background neutral temperature. The DSMC method correctly transfers one electron to the ion, changing the fast incident ion into a neutral particle and the former neutral particle into a CEX ion.

The calculation scheme for collision probabilities is the same for all processes under consideration, whereas cross sections require a more specific treatment. A collision of particle species i and j takes place if the stochastic probability fulfills the condition $P_{i,j} > n_r$ for a randomized number $n_r \in [0 \ldots 1]$:

$$P_{i,j}(\Delta v) = 1 - e^{-\Delta v \Delta t \sigma_{ji} n_j} \tag{9}$$

Cross sections for elastic collisions between ions are calculated by applying the model by Oh [5]:

$$\sigma_{\text{el}}(\Delta v) = \frac{k}{\Delta v} \tag{10}$$

where k is a constant.

Frequencies for CEX collisions have a highly nonlinear dependence on temperature and density. The usual approach is to fit experimental curves by polynomials of high degree, as has been reviewed by Szabo [3]. For practical purposes, simple stochastic approximations have been derived for the calculation of cross sections. Our previous model [6] used the CEX cross sections as measured by Rapp and Francis [7]. Here, we use the more recent measurements by Miller et al. [8] where the cross section is modeled by

$$\sigma_{\text{CEX}}(\Delta v) = a - b \ln \Delta v \tag{11}$$

where the two constant parameters a and b are derived by fitting experimental curves [9]. The collision probability is then computed with Eq. (9). Cross sections for the recombination of electrons with ions to form neutral particles are evaluated using a stochastic approach:

$$\sigma_{\text{re}} = k_{\text{re}} \sqrt{T_e} \tag{12}$$

where k_{re} is a constant. Table 1 summarizes the collision processes with the relevant models, and all coefficients.

One of the main tasks of SmartPIC has been the analysis of the spacecraft floating potential ϕ_f, which defines the differential potential between the spacecraft and the surrounding plasma environment. The configuration of positively biased surfaces surrounded by dielectrics, as which solar arrays can be seen, has been assessed in detail in a fully kinetic model by Hastings and Chang [2]. However, all these models are too complex to be applied in a large computational domain containing an entire satellite. Less sophisticated models suitable for this application have been introduced by Oh [5] and Samanta Roy [10]. These constitute the base of the present work.

The calculation of floating potentials is based upon the balance of electron and ion currents

$$I_E = I_N \tag{13}$$

Figure 4 gives a sketch of the complex plasma flows interacting with the spacecraft.

Fast Xe ions are expelled together with neutrals by the thruster, creating a positive ion exhaust current I_E. To counterbalance negative charging due to I_E, the neutralizer emits electrons I_N together with neutrals. In normal operation, these two cancel exactly. However, because CEX particles with energies far below 100 eV form a dense plasma cloud in the wake of the satellite, backflow currents play an important role, and the simple balance (13) has to be extended. Within an ambient plasma, the spacecraft is slightly negatively charged due to the higher mobility of the ambient electrons. Therefore, the CEX ions are drawn toward the satellite where they account for the ion backflow current $I_{B,I}$ and form a sheath [11].

This current is readily available in the simulation because discrete ions of charge multiplicity Z impacting the surface are counted to give

$$I_{B,i} = \frac{1}{\Delta t} \sum_k PPP_k Z_k e$$

The total ion current I_i balance introduced by Scharlemann et al. [12] consists of a thermal component $I_{\text{th},i}$, a ram current caused by ambient plasma flown through by the satellite with relative velocity v_{SC}, I_E, and I_B:

Table 1 Types of collisions implemented in SmartPIC

Type of collision	Model	Parameters	Reference
$Xe^+ + Xe \rightarrow^{\text{elastic}} Xe^+ + Xe$ $Xe^{2+} + Xe \rightarrow^{\text{elastic}} Xe^{2+} + Xe$	Eq. (10)	$k = 6.42 \times 10^{-16}$ $k = 1.28 \times 10^{-15}$	Tajmar et al. [4]
$Xe^+ + Xe \rightarrow^{\text{CEX}} Xe + Xe^+$ $Xe^{2+} + Xe \rightarrow^{\text{CEX}} Xe + Xe^{2+}$ $Xe^{2+} + Xe^+ \rightarrow^{\text{CEX}} Xe^+ + Xe^{2+}$	Eq. (11)	$a = 1.71 \times 10^{-18}$ s, $b = 1.18 \times 10^{-19}$ m $a = 1.03 \times 10^{-18}$ s, $b = 7.70 \times 10^{-20}$ m $a = 4.32 \times 10^{-19}$ s, $b = 2.80 \times 10^{-20}$ m	Miller et al. [8], Sakabe and Izawa [9]
$Xe^+ + e^- \rightarrow^{\text{recomb.}} Xe$	Eq. (12)	$k_{\text{re}} = 2.0 \times 10^{-18}$	Tajmar et al. [4]

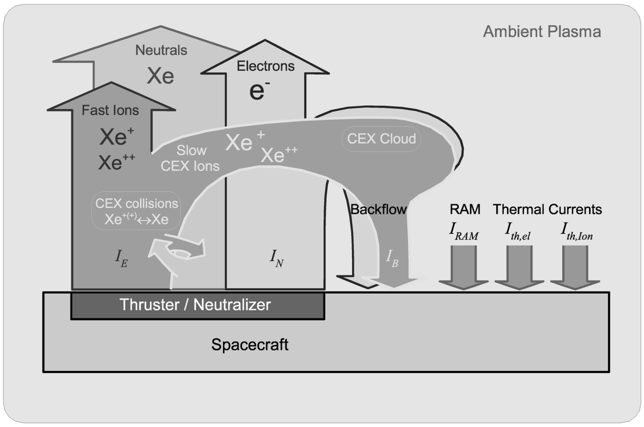

Fig. 4 Schematic of the plasma currents interacting with the spacecraft.

$$I_i = \frac{e \cdot n_0 \cdot A_{\mathrm{SC}}}{4} \cdot \sqrt{\frac{8 \cdot k_B \cdot T_{e0}}{\pi \cdot m_i}} + e \cdot n_0 \cdot v_{\mathrm{SC}} \cdot A_{\mathrm{RAM}} + I_{B,I} - I_E \tag{14}$$

where A_{SC} and A_{RAM} are the total area and ram area of the spacecraft, respectively, n_0 is the unperturbed ion density outside the sheath, and $T_{e0} = T_{i0}$ is the equilibrium plasma temperature.

This positive current has to be met by the electron current consisting of the ambient thermal current $I_{\mathrm{th},e}$, the backflow component $I_{B,E}$, and the known thruster neutralizer current, respectively,

$$\begin{aligned} I_e = -\frac{e}{4} \iint_{A_{\mathrm{SC}}} \mathrm{d}f \Bigg[n_{e0} \sqrt{\frac{8 k_B T_{e0}}{\pi m_e}} e^{\left(\frac{e(\phi_{\mathrm{SC}} - \phi_P)}{k_B T_{e0}}\right)} \\ + n_{\mathrm{CEX}} \sqrt{\frac{8 \cdot k_B \cdot T_{\mathrm{CEX}}}{\pi \cdot m_e}} \cdot e^{\left(\frac{e(\phi_{\mathrm{SC}} - \phi_{\mathrm{CEX}})}{k_B \cdot T_{\mathrm{CEX}}}\right)} \Bigg] + I_N \end{aligned} \tag{15}$$

The effect of secondary electron emission is not directly included but is taken into account via shielding coefficients that were fitted to the observed floating potential amplitudes as explained later. The first term is independent of thruster operation and depends solely on environmental plasma parameters n_{e0}, T_{e0} and the difference of spacecraft and plasma potentials $(\phi_{\mathrm{SC}} - \phi_P)$. In the second term, the locally varying backflow quantities n_{CEX} and T_{CEX} enter. However, the most important factors are the exponential functions depending upon the relative potential of the satellite with respect to the surrounding gas. These imply that a negatively charged object immersed in plasma with $(\phi_{\mathrm{SC}} - \phi_P) < 0$ draws only negligible electron currents. On the other hand, the positively biased interconnector structures between the solar cells have $(\phi_{\mathrm{SC}} - \phi_{\mathrm{CEX}}) > 0$, for which one has to abandon the exponential due to saturation and replace it by unity. They therefore draw large currents being limited solely by space charge effects around the contact points which, in this case, are geometrically small. Hence, related to the relevant surface area, the positively charged interconnectors draw a disproportionate current compared to the respective current collected by the large, negatively charged bulk of the satellite.

The value for the floating potential can then be determined by varying ϕ_{SC} in Eq. (15) until the condition $I_i = I_e$, which replaces Eq. (13), is met. Determination of I_e is a delicate issue [13] because the electrons are represented only by $n_e = n_i$ which is violated within the sheath. The latter one extends 5–10 D lengths $\lambda_D = \sqrt{\varepsilon_0 k_B T_{e0} / n_{e0} e^2}$ from all surfaces into the plasma. However, according to Hastings and Chang [2], the surface potentials are shielded to a far extent by space charge. Therefore, in the simulation, a constant shielding coefficient $\eta_{\mathrm{sh,[ic,diel]}}$ has been introduced to cut down the surface potentials on interconnectors (index "ic") and glass coverings (index "diel"), respectively. The equilibrium values for the unperturbed densities, potentials, and temperatures in Eqs. (14) and (15) are approximated by the respective values in the vicinity of the surfaces. Although this may physically not be well founded, the results in Sec. VI.E justify this approach.

B. Computational Model

SmartPIC is a single-workstation code. Therefore, it has to cope with the usual restrictions in memory and computational power. To be compliant with this specification, a fast multigrid solver technique requiring a special kind of grid has been chosen for field calculations. This allows for nearly instant solutions of the Laplace equation, high spatial resolution, and low memory consumption.

Because of the high symmetry of SMART-1 in the Y direction, the simulation includes only half of the satellite. The domain extends at least 0.5 m from the satellite into space. Boundary effects at the borders of domains have not been observed. The influence of the domain size has been investigated previously [4] and was found to be negligible. The size and shape of the domain is depicted in Fig. 5. The satellite is situated in the middle with the thrusters on the left. The domain sizes are $(Lx, Ly, Lz) = (2.2, 7.5, 2.2\ \mathrm{m})$. The z offset is varied at runtime according to the rotation of the solar array between 825 and 1100 mm.

The semi-adaptive multigrid allows for adaptation of the spatial resolution according to λ_D near the thruster exit and the fine interconnector structures and potentials in the vicinity of the solar array. The prefix "semi" indicates that the grid is not rotated with the solar array but adapts its local high-density structure instead, as can be seen in Fig. 6. The spatial resolution is varied in six steps from 8.59 to 275.00 mm. In that way, high local resolution and a minimized total number of grid cells can be achieved.

Propagation of the ions is achieved by an implementation of the "leap frog" scheme that can be found, for example, in [14]. The time steps Δt are determined by the condition that particles must not pass a distance Δx greater than one grid cell per time step. Hence, Δt is adapted in dependence on the local grid size. A great effort has been made to achieve the calculation of floating potentials according to Eqs. (14) and (15). As has been stressed earlier, it is of vital importance to get correct estimates for the electron current dominated by the free plasma potentials ϕ_P and ϕ_{CEX} in the vicinity of the solar panels. Hastings and Chang [2] have pointed out that the buildup of space charge in front of surfaces creates an effective shielding of potentials propagating into space. Because such plasma effects cannot be included in SmartPIC due to omnipresent quasi neutrality, a so-called shielding factor η_{sh} has been introduced to reduce effective surface potentials, where $\eta_{\mathrm{sh}} = 100\%$ means total shielding which corresponds to a surface potential of 0 V relative to spacecraft ground. The physical situation is very different for dielectric surfaces, such as glass coverings, and metallic structures, such as interconnector lines. Hence, two separate shielding coefficients indexed diel and ic, respectively, are used. Figure 7 shows the solar array potential distribution for different factors $\eta_{\mathrm{sh,diel}}$ and $\eta_{\mathrm{sh,ic}}$ as follows. Figure 7a shows an unshielded panel with $\eta_{\mathrm{sh}} = 0$. In Fig. 7b, only the glass surfaces are shielded by $\eta_{\mathrm{sh,diel}} = 50\%$. Figure 7c views a strongly shielded array with $\eta_{\mathrm{sh,diel}} = 50\%$ and $\eta_{\mathrm{sh,ic}} = 30\%$. According to Hastings and Chang [2], dielectric surfaces accumulate charge carriers at their surfaces leading to $\eta_{\mathrm{sh,diel}} = 50$–$100\%$, depending upon the surface potential. Total

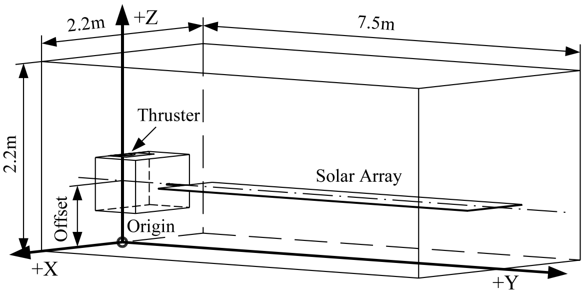

Fig. 5 Computational domain: position of the spacecraft relative to the domain.

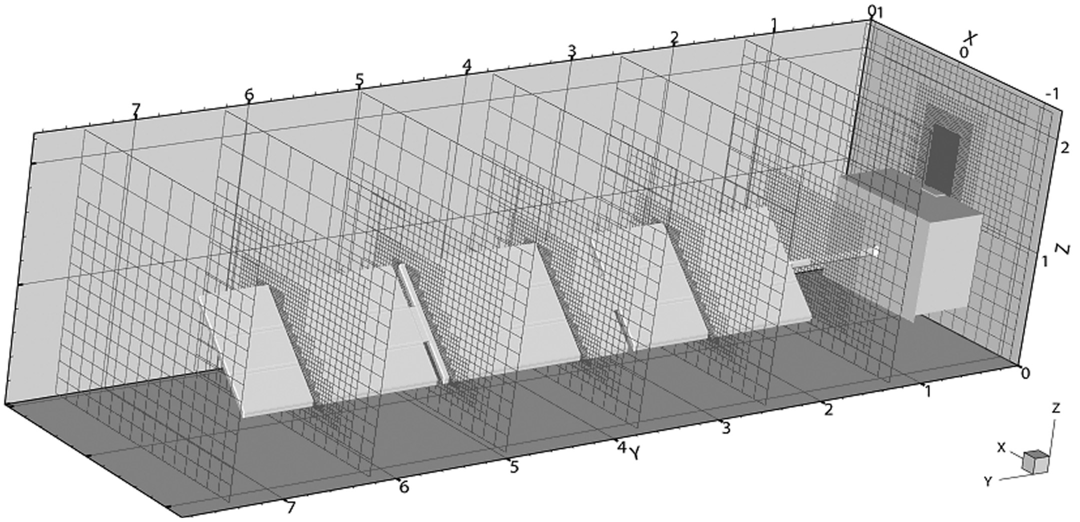

Fig. 6 Computational domain with representative grid slices.

shielding is given for low voltages and large distances to conductive surface parts. Hastings and Chang [2] report the existence of a snapover effect at >74 V relative to the plasma at which the shielding is reduced dramatically. Such high potentials are never reached on the solar panels of SMART-1, which justifies selection of high shieldings $70\% < \eta_{\mathrm{sh,diel}} < 100\%$. Conductive materials are shielded solely by space charge building up as soon as current flows to the surfaces. Therefore, the reduction of the effective conductor potential cannot be derived directly from the surface potentials because these result in $\eta_{\mathrm{sh,ic}} \sim 0$, as given by Hastings and Chang [2]. However, because SmartPIC works with finite sized grids, the space charge effect may be projected onto the surface without introducing large errors. In fact, interconnector shielding is a fit parameter but has to be small, as is known generally from langmuir probes. In SmartPIC, $\eta_{\mathrm{sh,ic}} = 0$–$20\%$ has been chosen. This value has been fitted to meet the floating potential amplitude measured on SMART-1.

Regarding the floating potentials, it is necessary to adapt the spacecraft ground $\phi_{\mathrm{sc}} = \phi_f$ to negative values while the far-field plasma is kept at $\phi_{P,0} = 0$ V. Therefore, the interconnector lines, which are at a potential of $\phi_{\mathrm{sc}} + [0$–$50]$ V, are partially negative and partially positive. This in turn has a major influence on the floating potential (see Sec. VI.E). To verify the simulation and to compare real-world measurement data with simulation outputs, so-called virtual instruments have been implemented [1]. These include Faraday cups, LP, and RPA sensors.

The spacecraft potential and electron and dust experiment consists of two cylindrically shaped metallic sensors (10 cm long with a diameter of 2 cm). Each sensor is mounted on the tip of a 60-cm-long boom on the $+X$ and $-X$ side of the spacecraft main body. SPEDE can operate in two modes, as a langmuir probe and as an electric field probe. In the langmuir probe mode, the sensor is biased (with respect to the spacecraft floating potential) with either a constant biasing voltage (to obtain the relative variation of the electron density) or a variable biasing voltage to obtain electron densities and temperatures of the surrounding plasma.

During the SMART-1 mission, some anomalies in the SPEDE current measurements were observed (see Sec. VI.C). It was therefore decided to use the capabilities of SmartPIC to investigate this issue in more detail. Some concessions had to be made to simulate the probes in SmartPIC, including a rectangular representation of SPEDE probes, which in reality are spherical in shape [12].

V. Verification

The plasma flow parameters have been verified with the help of vacuum chamber ground tests [4]. Originally, these experiments were part of a ground-test campaign for the French Stentor satellite that was lost in the 2002 Ariane-5 launch failure. The measurements have been conducted with a SPT-100 Hall thruster in the PIVOINE facility of Aerothermique Laboratory, operated by LABEN Proel based in Orleans, France [4,15]. Because the main characteristics of the SPT-100 and the PPT-1350 thrusters are very similar, operation of a SPT-100 at 350 V discharge voltage was considered representative of conditions for the PPT-1350.

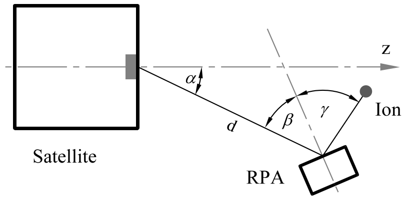

Fig. 8 Geometric configuration in Stentor ground tests.

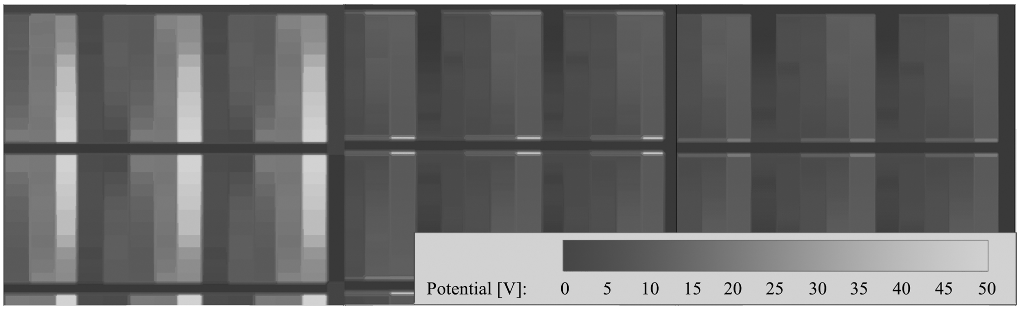

a) b) c)

Fig. 7 Detailed views of the solar array potential distribution for different shielding factors: a) $\eta_{\mathrm{sh}} = 0$, b) $\eta_{\mathrm{sh,diel}} = 50\%$, $\eta_{\mathrm{sh,ic}} = 0$, c) $\eta_{\mathrm{sh,diel}} = 50\%$, $\eta_{\mathrm{sh,ic}} = 30\%$.

Table 2 Geometrical positions of RPA sensors taken for comparison with simulation

Position	d, mm	α, deg	β, deg
1	670	10.0	0.0
2	670	0.0	0.0
3	670	5.0	0.0
4	670	10.0	0.0
5	670	15.0	0.0
6	670	20.0	0.0
7	1092	21.5	0.0
8	1035	11.2	0.0
9	1016	0.0	0.0
10	800	60.0	0.0
11	215	88.0	61.0

The test configuration consisted of a combined RPA and LP instrument similar to EPDP that was positioned at different distances and angles relative to the thruster. Figure 8 shows the geometric setup. Table 2 gives the respective values for all test sets that have been used.

Because of the grounding configuration (the first grid of the RPA was grounded to the satellite which results in an additional acceleration of the ions from the potential difference between the local plasma and the spacecraft potential), the experimental data had to be offset by +25 eV. The results of a sweep at low angles $-10 < \alpha < +20$ deg and the short distance of positions 1–6 are compiled in Fig. 9. Regarding peak energies, the simulation fits the experimental data well within the given error bars. Full widths at half-maximum (FWHM) values are considerably lower in the simulation output. This is reasoned by the constant initial energy of the ions discussed earlier in Sec. IV.A. Very good agreement can be observed for the larger distance positions 7, 8, and 9 in Figs. 10a–10c. Peak energies are met within ±10 eV. The higher offset in Fig. 10c at position 9 can be explained by a potential offset error in the ground-test data. The black vertical line in this graph marks the peak value of 332 eV given in the Laben report [15] for this position and the low-angle sweep. Complete sets of experimental data are shifted by approximately 25 eV relative to this line.

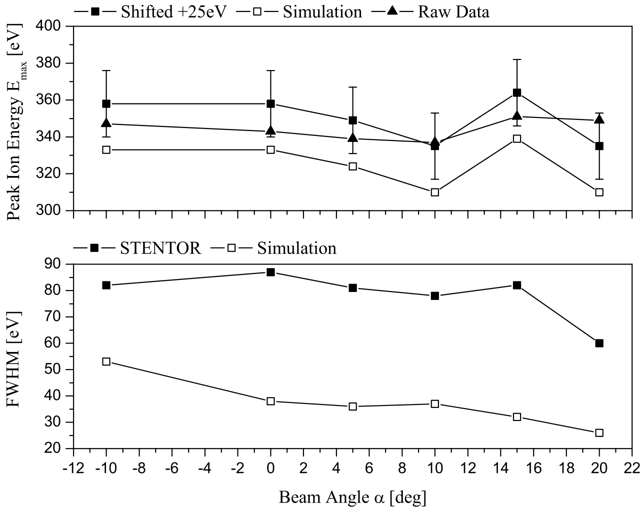

Fig. 9 Summarized RPA Results for the Angle Sweep Test at a Constant Distance of 670 mm.

For comparison, the corresponding (670 mm) low-distance graphs have been included in Fig. 10 as scattered lines. Data for different separations principally match up to a slight energy shift of 2–7 eV to higher energies at lower distances: a fact that can also be observed in the ground-test data and is explained by low-angle scattering within the beam.

High-angle measurement data have been used to verify the scattering model of the simulation. Figure 11 shows the results for position 10. The match between experiment and simulation is excellent. A clearly pronounced low-energy CEX peak at 6 eV dominates the spectrum of which a magnified view is shown in the insert. The little hump at ~300 eV is most likely a result of elastic scattering of ions and neutrals. In contrast to the low-angle tests, not only the simulated peak energy but also the FWHM is met. This is clear from the fact that the energy of CEX particles is mainly determined by the potential difference between their point of creation in the beam and the RPA potential, but not by the initial ion energy.

VI. Results

Data generated during continuous operation of the EPDP and SPEDE instruments has been used for additional calibration of the code to the specific configuration of SMART-1. Indirect measures like variations of the floating potential that had been missing a physical explanation could be demystified by thorough analysis of SmartPIC data.

A. Retarding Potential Analyzer Data

Based on the extreme instrument position at $d = 570$ mm and $\alpha = 85$ deg relative to the thruster exit, EPDP energy spectra are representative for the CEX environment. Unfortunately, no information about the actual tilting angle β is available. However, because the peak energy is a strong function of the angle of incidence, it was possible to fit the tilting to $\beta \sim 20$ deg by parametrizing the simulation.

Figure 12 shows simulation results and in-flight data for EPDP RPA spectra. A parasitic grounding offset of 11–18.5 eV has to be considered for all EPDP data, again due to the ground of the first grid of the RPA to spacecraft. For the STENTOR ground-test verification, this offset was constant at +25 V, as discussed in Sec. V, however,

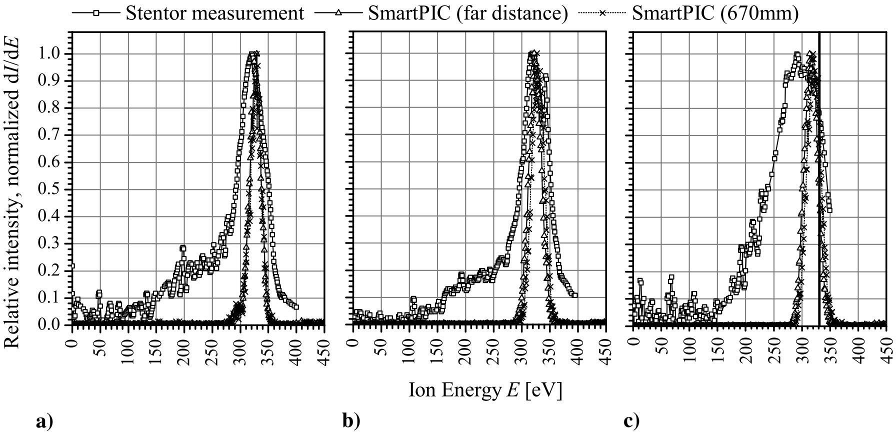

Fig. 10 Comparison of far distance ground test RPA data (exp) against simulation results (sim) for similar angles: a) exp: position 7, sim: positions 6 and 7; b) exp: position 8, sim: positions 4 and 8; c) exp: position 9, sim: positions 2 and 9.

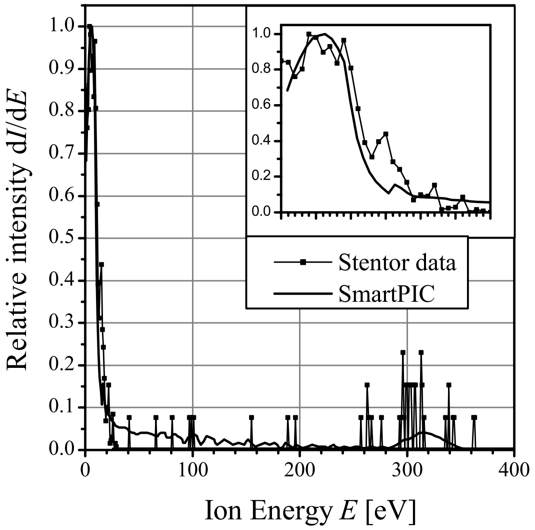

Fig. 11 Comparison of simulation and experiment at position 10.

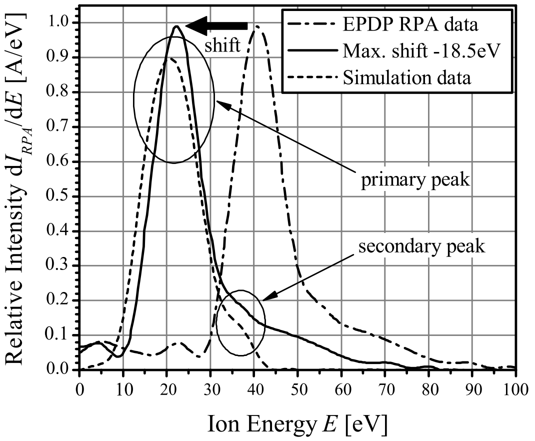

Fig. 12 CEX energy spectra for the SMART-1 EPDP RPA configuration. All data is 20-point fast Fourier transform smoothed.

here the reference is the spacecraft floating potential that does vary and hence the grounding offset can vary as well. The range of the resulting shift in the spectra is indicated in the figure by curves representing minimum and maximum. SmartPIC data show an average offset of 20.3 ± 1 eV to lower energies, which is slightly out of the announced shift range. According to King and Gallimore [16], a secondary peak due to the reaction $Xe^{2+} + Xe^{+} \rightarrow Xe^{+} + Xe^{2+}$ has to be expected at twice the energy of the primary one. The expected secondary peak in simulation results in Fig. 12 can be located at ~37 eV, which is 4.8 eV below the expected position. However because in-flight data show even greater deviations from the 1:2 ratio of primary and secondary peaks, this may indicate that the maximum shift on SMART-1 data had to be set to 22.5 V instead of 18.5 V. In this case, SmartPIC perfectly meets flight data within the respective variation.

Regarding the shape of the spectra, FWHM values compare well with 15.0 ± 0.5 eV for the simulation and 13.5 eV for in-flight data. A small high-energy tail below 100 eV can be observed in SMART-1 data that are not seen in simulation output. A possible explanation can be given by very low-energetic primary beam ions, or combined CEX and elastic scattering between ions and neutrals in the beam, which is not included in the collision model.

B. Flowfield Analysis

In SmartPIC, 3-D density data are available for all plasma species. This has proven to be very valuable, for example, when analyzing the propagation of CEX particles. Figures 13a and 13b show XZ slices of the number density of beam ions and singly charged CEX, respectively. The clustered appearance in the central region of the beam is a result of the necessary high PPP ratio which leads to some numerical noise. Therefore, the white specks are numerical artifacts and do not indicate regions of zero density. The figures show a clear asymmetry of the flowfield. In the vicinity of the thruster exit, both ion and CEX densities are higher by at least 1 order of magnitude on the right side, which corresponds to the $-X$ direction. At the position of the neutralizer on the right ($-X$) side of the thruster, the neutral density takes its maximum. Bearing in mind the exponential dependence of the collision probability in Eq. (9) upon species densities, it is clear that this position is the main source of CEX particles. This fact is mirrored by Fig. 13b where a jet of CEX particles, starting at the neutralizer location and emerging to the right, can be observed: a fact that is of high importance in the analysis of SPEDE data give next. The diffuse spreading of CEX ions can be understood in terms of the electric plasma potential which, according to Eqs. (5–8), takes the form of a ridge with a height of ~20 V at the center of the beam. Electric fields force the beam to spread and push out slow ions radially.

C. Spacecraft Potential Electron and Dust Experiment Asymmetry

During the SMART-1 mission, it was observed that the current measurements in the two SPEDE probes differ from each other. In particular, the probe on the $-X$ panel always showed higher current values than the one on the opposite side [12]. Because of the axis-symmetric design of the Hall thruster, this was a rather unexpected result and it was decided to investigate this phenomenon in more detail with SmartPIC.

Figure 14 shows current measurements of the two SPEDE probes over time. The upper curve represents the current measured on the $-X$ side and the lower curve the one on the $+X$ side. On average, these two measurements differ by 120–150 nA. Simulations conducted with SmartPIC show the same effect; the current measurements on the $-X$ side is always higher. Although SmartPIC always predicts higher

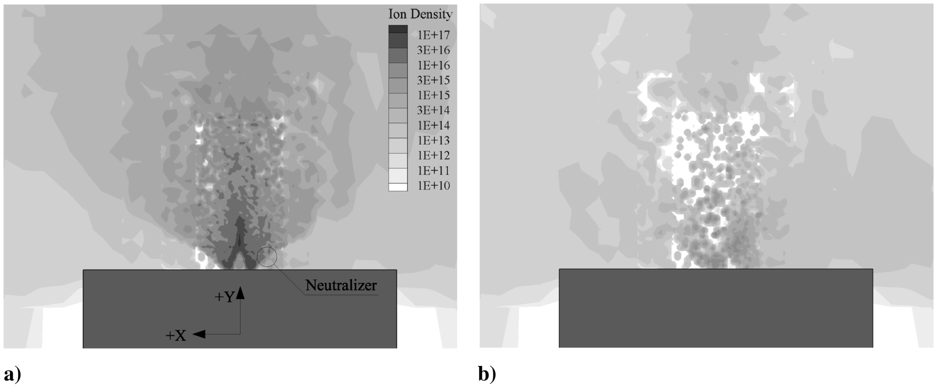

a) **b)**

Fig. 13 *XZ* cuts of the ion number densities through the thruster. The dark rectangle symbolizes the spacecraft's main body. The *X* axis runs from right to left with the origin at the center of the satellite: a) high-energetic beam ions, b) CEX ions.

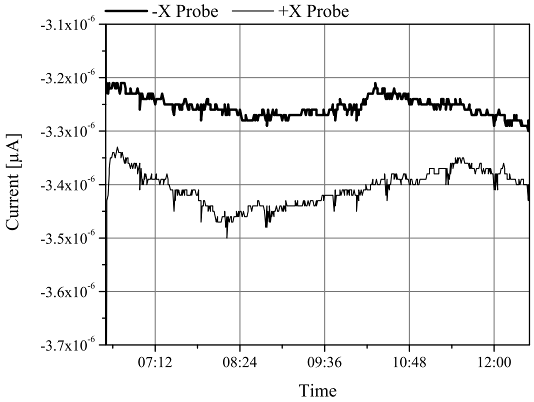

Fig. 14 SPEDE probe currents measured on-board of SMART-1 (biasing voltage +3 V), recorded on 10 Oct. 2003.

current differences (up to 330 nA), this numerical verification shows that the asymmetric current measurements are reasoned by a physical phenomenon rather than a simple problem with the spacecraft hardware or data analysis methods. The cause of this anomaly could only be found by a detailed investigation with SmartPIC. The software allows the researcher to produce a spatially resolved mapping of every particle species that is included in the numerical simulation. When investigating the distribution of CEX particles in the close vicinity of the thruster, an accumulation of CEX particles on one side of the thruster was found (see Fig. 13b). The origin of this accumulation is close to the location of the neutralizer and spreads over a relatively large volume of space which also includes the SPEDE probe on the $-X$ panel. Therefore, the SPEDE probe on the $-X$ panel is exposed to a much higher flux of charged particles than the probe on the other side, which obviously results in a higher current.

D. Backflow Distribution

As has already been pointed out earlier [1,4], the majority of backflow currents is collected by surfaces on the $+Z$ panel in the vicinity of the thruster. In the point of view of long-term operability and interplanetary missions, it is of great interest to have information about degradation of solar arrays which is increased by ion sputtering. Investigations regarding this topic have been conducted recently [4,13] and show clearly that solar arrays are subject to intense backflow. Figure 15 shows the ion backflow distribution onto front and back sides of the SMART-1 panels. On the glass-covered side of the arrays, only the positively biased metallic interconnector lines and structural elements are able to collect ions. The back side is unshielded biased to spacecraft ground potential. Intensities are moderate for horizontal positions around $\alpha = 0$ deg, when the front side faces the thruster. In the vertical position $\alpha = 90$ deg, the upper tip of the array leaves the wake of the spacecraft corpus masking out scattered beam ions. The array therefore receives intense backflow on the back side and the side faces of the array (not shown). Finally, at $\alpha = 180$ deg, the conductive back side, which attracts positive ions due to the negative ϕ_{SC}, draws high ion currents.

Analysis of particle trajectories shows that only very few ions reach the side faces of the main body. From this, one could deduce that it is possible to shield the arrays by arranging some kind of metallic deflector in the line of sight between the plume and the solar arrays.

E. Spacecraft Floating Potential

During the SMART-1 mission, SmartPIC has been used to study the variation of the ϕ_f and ϕ_{SC} with the orbital position. Monitoring of ion and electron backflow currents in the model Eqs. (14) and (15) showed that electron collection by the solar array is the driving factor of this effect.

The total ion currents in Fig. 16 show only little dependence upon the solar array tilt. At $\alpha = 90$ deg, the positive potentials emerging from the solar cells deflect a small amount of ions from the $+Z$ panel of the main body which corresponds to reduction from ~12 to 5 mA for that part. Backflow to the solar array rises for positions $\alpha >$ 90 deg because the conductive and grounded back side is an attractive collector compared to the glass-covered front side. On first sight, the influence of the solar panels, drawing less than 1 mA or for all positions, is negligible. However, this will be revised in the subsequent discussion.

Figure 17 shows the corresponding electron currents. Surprisingly, the interconnector structures, which have negligible size compared to the huge solar array panels or the main body faces, draw a rather high current. This can be understood when considering the second term on the right-hand side of Eq. (15). A positive bias of the interconnectors makes them very efficient current collectors. The exponential is replaced by unity and the current scales with the plasma density in the vicinity of the solar array. In Fig. 17, the interconnector current is high for angles $\alpha < 90$ deg when the glass side of the array faces the plume. In the vertical position, only the uppermost row of interconnectors reaches into the dense plasma region. Because $n_e = n_i$, the electron and ion densities are coupled; therefore, it is clear from the reduced amount of backflow at $\alpha = 90$ deg in Fig. 15 that the saturated electron backflow to the interconnectors, which scales with the plasma density, has to be small compared to that at $\alpha \approx 0$ deg.

At the same time (at $\alpha = 90$ deg), the ion backflow to the back side of the array rises, as can be seen in Fig. 16. Following the same argument as before, ion and electron densities are coupled, and I_e to the solar array is boosted despite the negative spacecraft ground ϕ_{SC} activating the negative exponential in Eq. (15). The back side alone cannot account for this effect, but the small side faces and conducting structures in between the interconnector lines are subjected to an intense backflow in this position.

When the array is turned to even greater angles $\alpha > 90$ deg, an increased number of ions make their way to the back side of the array. In contrast, the front side receives hardly any backflow. Thus, the electron current to the interconnectors is expected to vanish, leaving a missing ~10 mA in the current balance. The unchanged high interconnector current for $\alpha > 90$ deg in Fig. 17 can only be understood when taking into account a variable floating potential. Because of the negative ϕ_{SC}, ions are primarily attracted by grounded surfaces, which is obvious from Figs. 15 and 16. The latter one shows

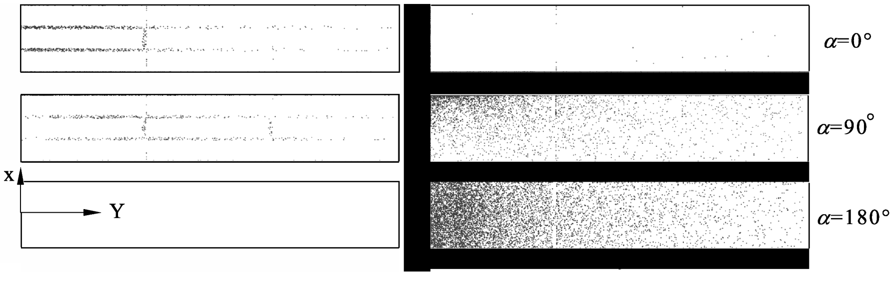

Fig. 15 Qualitative geometrical distribution of ion backflow currents on the solar arrays for tilting angles $\alpha = 0$, $\alpha = 90$ deg, and $\alpha = 180$ deg. The coordinate system indicates the origin of the panel at which it is mounted to the structure arm extending the main body (not shown).

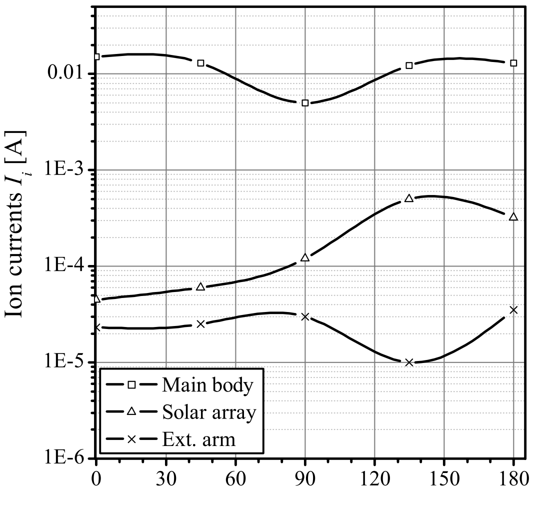

Fig. 16 Ion currents subdivided according to the geometric parts of the spacecraft for $\eta_{\mathrm{sh,diel}} = 0$ and $\eta_{\mathrm{sh,ic}} = 0$. Negligible backflow to the interconnectors is not shown.

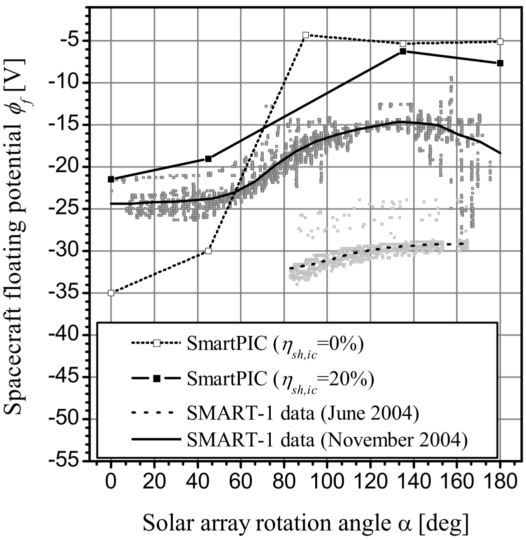

Fig. 18 Comparison of SmartPIC results for different interconnector shieldings and in-flight data from SMART-1 taken at different times.

an increase of the ion current to the solar array from negligible values at $\alpha < 90$ deg to approximately 0.5 mA at $\alpha = 135$ deg. This value is negligible compared to the total ion current of ~11.5 mA. For electrons, the main drain are the positive interconnector structures. However, because the plasma is neutral, the respective electron current cannot exceed the 0.5 mA of the ions. The only way to increase the global electron current to meet up with I_i is to allow a positive change in the floating potential of the spacecraft for $\alpha > 90$ deg. This is reflected by the curves in Fig. 18.

SmartPIC floating potential data are shown in comparison to in-flight measurements temporally separated by five months. The change in orbit from a high-altitude low Earth orbit toward free space during that time is responsible for the constant offset between the two experimental curves. The downward trend for the November data at $\alpha > 135$ deg is considered to be an artifact.

As discussed in Sec. IV.B, the shielding coefficient can be varied for glass surfaces and interconnectors differently. The effect of this setting can be seen in Fig. 18. Because of the negative floating potential at $\eta_{\mathrm{sh,diel}} = 70\%$ and $\eta_{\mathrm{sh,ic}} = 0\%$, more interconnectors have positive potential than for $\eta_{\mathrm{sh,ic}} = 20\%$ (see Sec. IV.B). Hence, for the premiere setting, the electron currents are generally higher for $\alpha < 90$ deg which induces a more negative floating potential necessary to balance electron and ion currents. This effect vanishes when the array is turned around to $\alpha > 90$ deg. In the latter position, regardless of the $\eta_{\mathrm{sh,ic}}$ setting, ion currents to the front side of the panel are negligible.

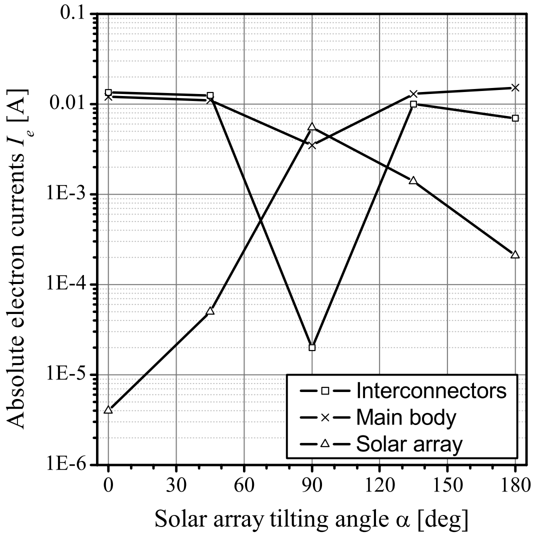

Fig. 17 Electron currents subdivided according to the geometric parts of the spacecraft for $\eta_{\mathrm{sh,diel}} = 0$ and $\eta_{\mathrm{sh,ic}} = 0$.

Again, we emphasize the dependence of the floating potential on the electron current. When the front side of the array faces the plume, and hence receives intense backflow, electron currents to the positively biased interconnectors are high. To balance ion and electron currents, it is necessary to lower the spacecraft floating potential which draws interconnectors having a bias voltage $< (-\phi_f)$ negative with respect to the plasma. These therefore leave the saturation state and receive exponentially small currents according to Eq. (15). The total electron current is reduced.

When the array is turned around such that the grounded back side faces the plume, the interconnectors do not receive high backflow anymore. To maintain an electron current that matches the ion backflow, it is necessary to raise the potential of the spacecraft relative to the plasma. The outermost interconnector lines (which still have access to the nearby flowing plasma striking the back side of the array) have to compensate the vanishing backflow in the center of the front side. Therefore, a much higher spacecraft potential is necessary at $\alpha > 90$ deg. In Fig. 18, the amplitude of the measured variation of ~10 V between $\alpha = 0$ and $\alpha = 135$ deg is best fit for values $\eta_{\mathrm{sh,ic}} \sim 20\%$.

From the preceding discussion and the variation of the floating potentials in the figure, it is clear that positively biased interconnector structures on the solar array, despite their small size compared to the rest of the satellite, play an enormous role for the spacecraft floating potentials.

VII. Conclusions

The SMART-1 mission represents a valuable opportunity to test innovative technologies on the schedule for future milestone missions. During a three-year period of close cooperation with ESA, a numerical simulation tool called SmartPIC was developed. The main purpose of this code is the detailed analysis of the reactive plasma environment created by the Hall thruster and interactions with the spacecraft. Virtual instruments that perfectly imitate the characteristics of onboard devices enable the calculation of realistic measurement results that can be compared directly to data obtained in experiments. This feature has extensively been used to verify the software against ground-test and in-flight data.

Analysis of the flowfield by tracking of single particles, as well as density information, enabled the identification of the relevant processes driving the plasma backflow to the spacecraft. Charge-exchange collisions within the plume create low-energetic ions that are radially pushed out of the beam. These particles are attracted by the negative ground potential of the spacecraft relative to the neutral plasma. On impact, they cause sputtering and other degradation effects that may harm sensitive electronic devices, but can also lead to sparking and subsequent failure of instruments and solar panels.

During in-flight measurements on SMART-1, an anomaly in the satellite's floating potential was observed. Investigation with SmartPIC revealed that small metallic interconnector lines biasing solar cells draw high electron currents due to their positive potential relative to the plasma. Depending upon the tilting angle of the solar array relative to the plume, the plasma backflow to the array varies. With the solar cells facing the exhaust, the spacecraft potential drops to −25 V due to increased interconnector electron currents. Turning the array by 180 deg faces the grounded conductive back side of the array to the plasma which dramatically reduces the interconnector current, and therefore leads to a more positive floating potential of −15 V.

Detailed three-dimensional data regarding densities, ion energies, potentials, plasma temperature, and backflow distributions helped to interpret measurement results of SMART-1 sensor packages. The simulation has been used to give valuable contributions to understand the interactions of electric propulsion-generated plasma and the spacecraft. Because of its great variability with respect to spacecraft geometry and the type of electric propulsion system, SmartPIC could readily be applied to support future missions.

Acknowledgments

This work was funded by the Austrian Space Agency under grant ASAP-CO-007/04. The authors greatly appreciate the support from J. Gonzalez del Amo, D. Estublier, A. Hilgers, and the ESA SMART-1 working group members.

References

[1] Tajmar, M., González del Amo, J., and Hilgers, A., "Modeling of Spacecraft Environment Interactions on SMART-1," *Journal of Spacecraft and Rockets*, Vol. 38, No. 3, 2001, p. 393.
doi:10.2514/2.3697

[2] Hastings, D. E., and Chang, P., "The Physics of Positively Biased Conductors Surrounded by Dielectrics in Contact with Plasma," *Physics of Fluids B*, Vol. 1, No. 5, 1989, p. 1123.
doi:10.1063/1.858982

[3] Szabo, J. J., Jr., "Fully Kinetic Numerical Modeling of a Plasma Thruster," Ph.D. Thesis, Massachusetts Inst. of Technology, Cambridge, MA, 2001.

[4] Tajmar, M., Meissl, W., González del Amo, J., Foing, B., Laasko, H., Noci, G., Capacci, M., Mälkki, A., Schmidt, W., and Darnon, F., "Charge-Exchange Plasma Contamination on SMART-1: First Measurements and Model Verification," AIAA Paper 2004-3437, July 2004.

[5] Oh, D., "Computational Modeling of Expanding Plasma Plumes in Space Using a DSMC Algorithm," Ph.D. Thesis, Massachusetts Inst. of Technology, Cambridge, MA, 1997.

[6] Tajmar, M., González, J., and Hilgers, A., "Modelling of Spacecraft Environment Interactions on SMART-1," AIAA Paper 2000-3526, July 2000.

[7] Rapp, D., and Francis, W. E., "Charge Exchange Between Gaseous Ions and Atoms," *Journal of Chemical Physics*, Vol. 37, No. 11, 1962, p. 2631.
doi:10.1063/1.1733066

[8] Miller, J. S., Pullins, S. H., Levandier, D. J., Chiu, Y., and Dressler, R. A., "Xenon Charge Exchange Cross Sections for Electrostatic Thruster Models," *Journal of Applied Physics*, Vol. 91, No. 3, 2002, p. 984.
doi:10.1063/1.1426246

[9] Sakabe, S., and Izawa, Y., "Cross Sections for Resonant Charge Transfer Between Atoms and Their Positive Ions: Collision Velocity ≤ 1 a.u.," *Atomic Data and Nuclear Data Tables*, Vol. 49, No. 2, 1991, p. 257.
doi:10.1016/0092-640X(91)90027-2

[10] Samanta Roy, R., "Numerical Simulation of Ion Thruster Plume Backflow for Spacecraft Contamination Assessment," Ph.D. Thesis, Massachusetts Inst. of Technology, Cambridge, MA, 1995.

[11] Hershkowitz, N., "Sheaths: More Complicated Than You Think," *Physics of Plasmas*, Vol. 12, No. 5, 2005, p. 055502.
doi:10.1063/1.1887189

[12] Scharlemann, C., Tajmar, M., González del Amo, J., Estublier, D., Noci, G., and Carpacci, M., "Influence of the Solar Arrays on the Floating Potential on SMART-1: Numerical Simulations," AIAA Paper 2005-3859, July 2005.

[13] Sedmik, R., Scharlemann, C., and Tajmar, M., "Numerical Simulation of the Interactions Between Solar Arrays and the Surrounding Plasma Environment," *Proceedings of the 29th International Electric Propulsion Conference*, Paper 2005-214, Oct. 2005.

[14] Tannehill, J. C., Anderson, D. A., and Pletcher, R. H., *Computational Fluid Mechanics and Heat Transfer*, 2nd ed., Taylor and Francis, Philadelphia, 1997.

[15] Stentor Ground Team, "Final Report for STENTOR Plasma Probe Extensive on Ground Characterization," Doc. No. TL 17106, LABEN S.p.A, Milan, Italy, Oct. 2000.

[16] King, L. B., and Gallimore, A. D., "Identifying Charge Exchange Collision Products Within the Ion-Energy Distribution of Electrostatically Accelerated Plasmas," *Physics of Plasmas*, Vol. 6, No. 7, 1999, p. 2936.
doi:10.1063/1.873251

J. Blandino
Associate Editor